Optoelectronic properties of monolayer molybdenum disulfide with sulfur vacancies

Robin Aydinonat
Bachelor's thesis

March 2021

Advisors:

Prof. Dr. rer. nat. Dr. h. c. Claudia Draxl,
Humboldt-Universität zu Berlin

Dr. Ronaldo Rodrigues Pelá,
Humboldt-Universität zu Berlin

Assoz. Prof. Dipl.-Ing. Dr. Peter Puschnig,
Karl-Franzens-Universität Graz

Abstract

Monolayer MoS_2 is known to exhibit outstanding optoelectronic properties such as an energy gap and thus photon absorption in the visible range, which make it a very interesting material for various applications including ultra-thin field effect transistors and solar cells [1, 2]. However, its remarkable characteristics may be affected by defects. This work is a theoretical study of the impact of sulfur vacancies on the optoelectronic properties of monolayer MoS_2. **exciting**, a full-potential all-electron LAPW code, is employed to perform *ab initio* calculations within density-functional theory and many-body perturbation theory at the level of G_0W_0 and the Bethe-Salpeter equation. It is observed that sulfur vacancies introduce defect-related states, narrowing the fundamental bandgap. Compared to the pristine material, the sulfur vacancies tend to redshift the absorption spectrum and to decrease its maximum intensity.

Contents

Abstract **2**

Acknowledgements **4**

1 Motivation **5**

2 Density-Functional Theory **6**

3 Many-body Perturbation Theory **7**
3.1 GW approach . . . 7
3.2 G_0W_0 approximation . . . 7
3.3 Bethe-Salpeter equation (BSE) . . . 8

4 The APW and LAPW methods **10**
4.1 The augmented plane-wave method (APW) . . . 10
4.2 The linearized augmented plane-wave method (LAPW) . . . 11
4.3 The LAPW+LO method . . . 12

5 Computational details **13**
5.1 Convergence tests and DFT calculations . . . 13
5.2 G_0W_0 calculations . . . 14
5.3 BSE calculations . . . 15

6 Results **16**
6.1 Structural properties . . . 16
6.2 Charge density distribution . . . 18
6.3 Electronic structure . . . 19
6.3.1 Kohn-Sham bandstructure . . . 19
6.3.2 G_0W_0 bandstructure . . . 24
6.4 Optical properties . . . 26
6.4.1 Absorption spectra . . . 26
6.4.2 Exciton wavefunctions in reciprocal and real space . . . 28

7 Summary **30**

Acknowledgements

I want to thank

- Prof. Peter Puschnig for helping me to establish contact to the Humboldt-Universität zu Berlin and to Prof. Claudia Draxl in particular. Also, his dissertation has been a benefit for the theoretical background of the present thesis.
- Prof. Claudia Draxl for proposing a very interesting topic to me, which gave me a fascinating introduction into several levels of theory of solid state physics, and for her supervision of the project.
- Dr. Ronaldo Rodrigues Pelá, with whom I had meetings almost every week during the time of working on this thesis, for sharing his knowledge and experience with me.
- the entire SOLgroup at the HU Berlin for a nice time in Berlin as well as for their kindness and helpfulness.
- my flatmates at the Studentendorf Adlershof, especially Jacob from Australia and Jingwen from China, for always having a good time with me.
- the European Union for the great Erasmus+ programme, which enabled my semester abroad.
- and last but not least, my parents for always supporting me, my friends for several Skype meetings during corona-lockdown evenings and my girlfriend Angela for her love and support.

1 Motivation

The isolation of graphene in 2004 [3], which then led to the award of the Nobel Prize in Physics in 2010, triggered a whole new field of research, namely the study of 2D materials. Especially two-dimensional transition metal dicalchogenides (2D TMDCs) are now of great interest to physicists and materials scientists because of the possibility to engineer their optoelectronic properties. In contrast to graphene being a semimetal, TMDCs are semiconductors. Since semiconductors play a significant role in today's technology and 2D TMDCs typically have energy gaps in the visible range, allowing for efficient emission and absorption of light, they are very promising materials for optoelectronic devices.

2D TMDCs have the chemical formula MX_2, where M is a transition metal (e.g. Mo or W) and X is a chalcogen atom (e.g. S, Se or Te). They are *quasi* two-dimensional, meaning that they consist of a layer of M atoms sandwiched between two layers of X atoms. The specific TMDC studied in the present thesis, MoS_2 (molybdenum disulfide), exists in both bulk and monolayer forms. Under normal conditions of pressure and temperature, the crystal structure of the monolayer is hexagonal, as can be seen in Fig. 1. Bulk crystals of MoS_2 consist of monolayers bound to each other by Van-der-Waals forces. The monolayers themselves are bound covalently. By mechanical exfoliation, it is possible to isolate one or several layers. The bandgap depends on the number of monolayers, and there is a transition of an indirect (as for the bulk) to a direct bandgap (as for the monolayer). The characteristic direct bandgap and strong exciton binding energies account for the outstanding optoelectronic properties of this 2D material [4, 5]. Recently, hybrid inorganic/organic systems, i.e. compounds of MoS_2 and organic semiconductors have become a very promising field of research [6].

Under normal experimental conditions, sulfur vacancy (SV) defects are prevalently existent due to the high volatility of the sulfur atoms. This makes sulfur vacancies one of the most common defects in MoS_2. It has been shown experimentally that these defects can lead to significant degradation in charge-carrier mobility affecting the photoluminescence spectrum [7]. With this in mind, this work is dedicated to theoretically study the impact of sulfur vacancies on the optoelectronic properties, with a specific focus on the electronic structure and the absorption spectrum.

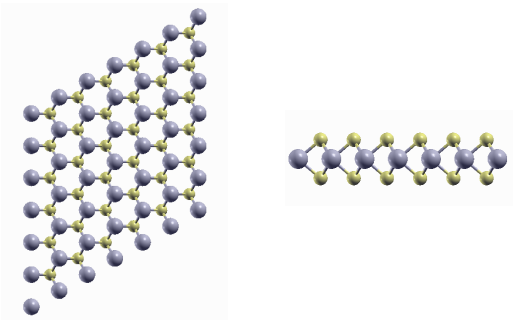

(a) (b)

Figure 1: (a) Top view of the MoS_2 monolayer with its characteristic honeycomb structure. S atoms are in yellow and Mo atoms in grey. (b) Side view of the MoS_2 monolayer, showing the layer of Mo atoms sandwiched between two layers of S atoms.

2 Density-Functional Theory

The approach for the ground-state calculations in this work is density-functional theory (DFT). This theory is based on the Hohenberg-Kohn theorems that were established in 1964. The central quantity in DFT is the electron density $n(\mathbf{r})$ in the ground-state that determines the external potential $v(\mathbf{r})$ of a bound system of interacting electrons uniquely. Furthermore, also the system's many-body wavefunction Ψ is a functional of $n(\mathbf{r})$.

In their paper, Hohenberg and Kohn describe the ground-state of an interacting electron gas in an external potential $v(\mathbf{r})$ by introducing a functional of the electron density $F[n(\mathbf{r})]$, independent of $v(\mathbf{r})$, and show that the energy functional

$$E = \min_{n(\mathbf{r})} \left\{ \int v(\mathbf{r}) n(\mathbf{r}) d\mathbf{r} + F[n(\mathbf{r})] \right\} \tag{1}$$

gives the ground-state total energy E of the system associated with $v(\mathbf{r})$. Being able to calculate Ψ and E from the electron density alone means that $n(\mathbf{r})$ contains all the information needed to solve the Schrödinger equation $\hat{H}\Psi = E\Psi$ of the electronic system. Therefore, knowing $n(\mathbf{r})$ gives access to the full Hamiltonian $\hat{H}$ of the system.

In 1965, Kohn and Sham established their *"Self-Consistent Equations Including Exchange and Correlation Effects"*. The Kohn-Sham (KS) scheme implements DFT in a way where the many-electron Schrödinger equation is split into a set of independent one-particle equations for the electronic wavefunctions, called KS equation, that reads for an electron i:

$$\left[\frac{-\nabla^2}{2} + v(\mathbf{r}) + V_H(\mathbf{r}) + V_{XC}(\mathbf{r}) \right] \psi_i(\mathbf{r}) = \varepsilon_i^{KS} \psi_i(\mathbf{r}) \tag{2}$$

where on the right-hand side ε_i^{KS} is the KS-eigenvalue of electron i and $\psi_\mathrm{i}(\mathbf{r})$ is the single-electron wavefunction, depending on only three spatial variables. On the left-hand side there are, apart from the kinetic energy operator, three potentials: v describes the interaction between one electron and the collection of all the atomic nuclei and V_H is the Hartree potential, describing the repulsion between electron i and the total electron density from all the electrons in the system. The exchange-correlation potential V_{XC} includes essentially all the many-body physics which is not incorporated in the other potentials.

It should be noted that the KS scheme is exact, apart from the approximation that has to be made for the exchange-correlation part. In this work, the generalized gradient approximation as introduced by Perdew-Burke-Ernzerhof (GGA-PBE) is used, which employs the electron density and its gradient to build the exchange-correlation potential [8].

The solution of the KS equation (Eq. 2) is a self-consistent process. One starts by defining an initial trial electron density which fixes the Hartree potential and then solves the KS equations to find the single-electron wavefunctions $\psi_i(\mathbf{r})$. Then, from these wavefunctions, the electron density is determined by

$$n(\mathbf{r}) = \sum_{i=1}^{N} |\psi_i(\mathbf{r})|^2 \tag{3}$$

where $\psi_i(\mathbf{r})$ are the electronic wavefunctions and N is the number of electrons. By comparing the trial electron density and the calculated electron density, the density for the next iteration step has to be updated [9, 10, 11]. These steps are gone through until the desired convergence target of the total energy is achieved. Convergence in this context means that the total energy should only change by a defined small amount (e.g. less than 10^{-6} Hartree) between consecutive iteration steps.

3 Many-body Perturbation Theory

3.1 GW approach

The GW approach is the state-of-the-art method used for calculating accurate electronic band-structures. In this context, the electrons in the material are described as quasiparticles (QP). QP are so-called elementary excitations; they describe the particle and the distortion it causes in its surroundings. This means i.a. that QP behave like electrons in free space with an effective mass different to the standard electron mass, caused by the interaction of the electrons with all the other electrons and nuclei [12].

GW is an approximation that enables to calculate the self-energy Σ of a many-body system of electrons. In the many-body system, the electrons screen the electrostatic repulsion between each other, leading to the screened Coulomb interaction W that is weaker than the bare Coulomb interaction. This screening affects the propagation of the QP, which is described by a one-body Green's function G. More detailed, this propagator function G gives the probability amplitude for the propagation of the particle between two distinct quantum states. The expansion of Σ in terms of G and W is truncated after the first term; thus leading to the product

$$\Sigma \approx iGW. \tag{4}$$

3.2 G_0W_0 approximation

The G_0W_0 approximation features no self-consistency but is rather a single-shot calculation applied as a perturbative correction to the KS eigenvalues. Since, in general, the one-body Green's function G is unknown, one can approximate it by a non-interacting propagator operator G_0. Furthermore one can make use of W_0, the dynamically screened Coulomb potential built within the random-phase approximation (RPA) [13, 14, 15]. Finally, the DFT eigenvalues can be corrected by a term containing the self energy $\Sigma \approx iGW$ [16]. After Fourier transformation to reciprocal space, Hedin's equation has the form

$$\Sigma(\mathbf{r}, \mathbf{r}'; \omega) = \frac{i}{2\pi} \int G_0(\mathbf{r}, \mathbf{r}'; \omega + \omega') W_0(\mathbf{r}, \mathbf{r}'; \omega') e^{i\omega'\eta} d\omega' \tag{5}$$

where G_0 is the non-interacting propagator operator, given by

$$G_0(\mathbf{r}, \mathbf{r}'; \omega) = \sum_{n\mathbf{k}} \frac{\psi_{n\mathbf{k}}(\mathbf{r}) \psi_{n\mathbf{k}}(\mathbf{r'})}{\omega - \tilde{\varepsilon}_{n\mathbf{k}}} \tag{6}$$

with $\tilde{\varepsilon}_{n\mathbf{k}} = \varepsilon^{KS}_{n\mathbf{k}} + i\eta\, sgn(\varepsilon_F - \varepsilon^{KS}_{n\mathbf{k}})$. Here, ε_F is the Fermi energy and η is an infinitesimally small positive number. The propagating electron has energy $\varepsilon^{KS}_{n\mathbf{k}} > \varepsilon_\mathrm{F}$, whereas the hole has energy $\varepsilon^{KS}_{n\mathbf{k}} < \varepsilon_\mathrm{F}$. The screened Coulomb potential is given by

$$W_0(\mathbf{r}, \mathbf{r}'; \omega) = \int \varepsilon^{-1}(\mathbf{r}, \mathbf{r_1}; \omega) v_C(\mathbf{r_1}, \mathbf{r}') d\mathbf{r_1} \tag{7}$$

where $v_C(\mathbf{r}, \mathbf{r}') = 1/|\mathbf{r} - \mathbf{r}'|$ is the bare Coulomb potential and $\varepsilon(\mathbf{r},\ \mathbf{r'};\ \omega)$ is the dielectric function calculated in the RPA [17]. With equations 6 and 7, the self energy (Eq. 5) can be evaluated and finally the quasiparticle eigenvalues are

$$\varepsilon^{QP}_{n\mathbf{k}} = \varepsilon^{KS}_{n\mathbf{k}} + Z_{n\mathbf{k}}[\Re\, \Sigma_{n\mathbf{k}}(\varepsilon^{KS}_{n\mathbf{k}}) - V^{XC}_{n\mathbf{k}}] \tag{8}$$

where $\Sigma_{n\mathbf{k}}$ and $V^{XC}_{n\mathbf{k}}$ are the diagonal matrix elements of the self-energy and the exchange-correlation potential, respectively. $Z_{n\mathbf{k}}$ is a renormalization factor [18].

3.3 Bethe-Salpeter equation (BSE)

While the *GW* approximation is used to describe one-particle excitations of electronic systems, e.g. observed with photo-electron emission, the Bethe-Salpeter equation (BSE) is a tool to treat *two*-particle excitations in solids. These phenomena occur, when incident photons create electron-hole pairs in the material. Electron-hole pairs are called *excitons*. Electron and hole are bound by their attractive Coulomb interaction.

In the absorption spectra of materials, it is possible to observe peaks corresponding to photon energies just below the bandgap, where the material might be expected to be transparent. These absorption features arise from bound excitons. Their binding energies are given as the difference between the energy required to create an exciton and the energy required to create a free electron and a free hole [19].

The BSE is the equation of motion for the two-particle correlation function [20, 21]. In the proper basis [22, 23], the solution of the Bethe-Salpeter equation for the two-particle correlation function S can be found by solving an effective eigenvalue problem

$$H^{eff} A^{\lambda} = E^{\lambda} A^{\lambda} \tag{9}$$

with the effective Hamiltonian

$$H^{eff} = H^{diag} + 2\gamma_x H^x + \gamma_c H^c \tag{10}$$

consisting of the diagonal part, H^{diag}, that describes the independent particle transitions, the repulsive exchange term, H^x, caused by the unscreened Coulomb interaction, and the attractive term, H^c, that accounts for the electron-hole correlations caused by the screened Coulomb potential. The factor 2 in front of H^x is there for the spin multiplicity, and γ_x and γ_c can be used to describe either the spin-singlet ($\gamma_x = \gamma_c = 1$) or spin-triplet ($\gamma_x = 0$ and $\gamma_c = 1$) [23].

Using the eigenvalues E^{λ} (i.e. the excitation energies) and the eigenvectors A^{λ} (that give information about the composition of the λ-th excitation), each element of the two-particle correlation function S can now be expressed as

$$S_{vc\mathbf{k},v'c'\mathbf{k}'} = i \sum_{\lambda} \frac{A^{\lambda}_{vc\mathbf{k}} [A^{\lambda}_{v'c'\mathbf{k}'}]^*}{\omega - E^{\lambda}} \tag{11}$$

where v, c, and $\mathbf{k}$ label the valence states, conduction states, and $\mathbf{k}$-points, and ω is the frequency.

The Tamm-Dancoff-approximation (TDA) [24] neglects the coupling between the resonant (reflecting excitations) and anti-resonant (reflecting de-excitations) components of the Hamiltonian. Now, the parts of the effective Hamiltonian can be expressed as follows:

$$H^{diag}_{vc\mathbf{k},vc\mathbf{k}'} = (\varepsilon_{c\mathbf{k}} - \varepsilon_{v\mathbf{k}}) \delta_{vv'} \delta_{cc'} \delta_{\mathbf{k}\mathbf{k}'} \tag{12}$$

where $\varepsilon_{n\mathbf{k}}$ is the single particle energy of the n-th band.

$$H^{x}_{vc\mathbf{k},v'c'\mathbf{k}'} = \int d^3\mathbf{r} \int d^3\mathbf{r}' \Phi_{vk}(\mathbf{r}) \Phi^*_{c\mathbf{k}}(\mathbf{r}) v_C(\mathbf{r},\mathbf{r}') \Phi_{v'\mathbf{k}'}(\mathbf{r}') \Phi^*_{c'\mathbf{k}'}(\mathbf{r}') \tag{13}$$

where $v_C(\mathbf{r},\mathbf{r}')$ is the short-range Coulomb potential. The above exchange Hamiltonian describes the repulsive exchange interaction between two electron-hole pairs at **r** and **r'** respectively [25].

$$H^c_{vc\mathbf{k},v'c'\mathbf{k}'} = -\int d^3\mathbf{r}\int d^3\mathbf{r}'\Phi_{v\mathbf{k}}(\mathbf{r})\Phi^*_{c\mathbf{k}}(\mathbf{r}')W(\mathbf{r},\mathbf{r}')\Phi_{v'\mathbf{k}'}(\mathbf{r})\Phi^*_{c'\mathbf{k}'}(\mathbf{r}') \tag{14}$$

with the screened Coulomb potential $W(\mathbf{r},\mathbf{r}')$.

Now, if we want to calculate the macroscopic transverse dielectric tensor $\varepsilon_M(\omega)$ from the BSE solutions, we can obtain it in the optical limit ($\mathbf{q}=0$, i.e. no momentum transfer). The imaginary part of this tensor is proportional to the product of the frequency-dependent index of refraction $n(\omega)$ and the extinction coefficient $k(\omega)$ [26]. In the range of interest for optical measurements in semiconductors, $n(\omega)$ is generally nearly constant. Therefore, the imaginary part of the dielectric tensor can be considered proportional to the extinction coefficient, that quantifies the absorption spectrum:

$$\Im[\varepsilon_M(\omega)] \equiv 2n(\omega)k(\omega) \approx 2\sqrt{\epsilon_0}k(\omega) \tag{15}$$

Here, ϵ_0 denotes the dielectric constant in the optical frequency range above the lattice-mode frequencies and is assumed to be independent of ω [27].

From the BSE solutions, the imaginary part of the dielectric function is obtained using

$$\Im[\varepsilon^i_M(\omega)] = \frac{8\pi^2}{V}\sum_\lambda |t_{\lambda,i}|^2\delta(\omega - E_\lambda) \tag{16}$$

where V is the unit cell volume. The transition coefficients $t_{\lambda,i}$ are

$$t_{\lambda,i} = \sum_{vc\mathbf{k}} A^\lambda_{vc\mathbf{k}}\frac{\langle v\mathbf{k}|\hat{p}_i|c\mathbf{k}\rangle}{\varepsilon_{c\mathbf{k}} - \varepsilon_{v\mathbf{k}}}, \tag{17}$$

$\hat{p}$ is the momentum operator and i labels the polarization components x, y and z.

4 The APW and LAPW methods

4.1 The augmented plane-wave method (APW)

There are several methods for solving the Kohn-Sham equations for periodic crystals. Essentially, they differ in the choice of the basis set used for constructing the single-particle wavefunctions. For problems with periodic boundary conditions, the most intuitive choice would be using plane waves $e^{i(\mathbf{k}+\mathbf{G})\mathbf{r}}$ as basis functions. Here, $\mathbf{k}$ is a wave vector in the first Brillouin zone and $\mathbf{G}$ is a reciprocal lattice vector. However, there is a big disadvantage of this method: for achieving a good description of the wavefunctions near the atomic nuclei, there are so many plane waves needed that the computational costs increase tremendously. This problem motivated the development of the augmented plane wave (APW) method in 1937 by Slater [28, 29, 30]. The idea is, that close to the atomic nuclei, the potential as well as the wavefunctions are comparable to the well-known ones in an isolated atom. Therefore Slater exerted an augmentation of the plane-waves in the surroundings of the atomic nuclei, by using atomic-like functions within the so-called *muffin-tin spheres*. These spheres are centered at the nuclei positions. He kept using plane waves in the *interstitial region*, i.e. the region between the muffin-tin spheres. It is important that the muffin-tin spheres do not overlap, i.e. the sum of the muffin-tin radii of every two atoms in the cell must be smaller than their distance. The wavefunctions are approximately spherical and strongly varying within the muffin-tin spheres. On the other hand, within the interstitial region, wavefunctions and potential are less varying [31]. A visualization of the partitioning for two atoms in a unit cell can be found in Fig. 2.

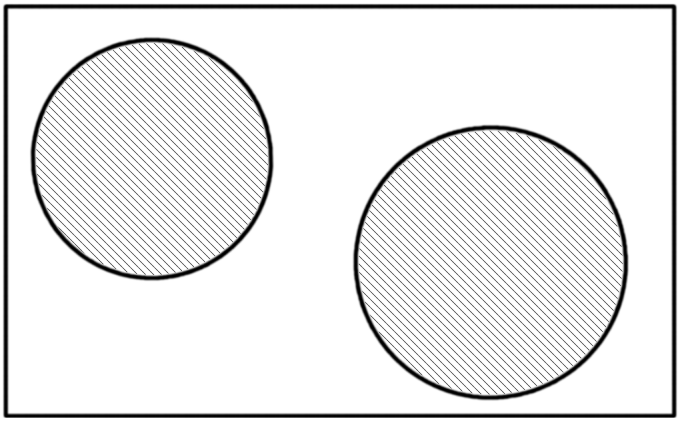

Figure 2: Visualization of the partitioning using the example of a unit cell containing two atoms. The muffin-tins are located within the hatched circles and the rest of the rectangular cell is the interstitial region.

Mathematically, the basis expansions used for the two different regions are therefore radial solutions of the Schrödinger equation for the spherical muffin-tin region (M) and plane waves for the interstitial region (I):

$$\varphi(\mathbf{r}) = \begin{cases} \Omega^{-1/2} e^{i(\mathbf{G}+\mathbf{k})\mathbf{r}} & \mathbf{r} \in I \\ \sum_{lm} A_{lm} u_l(r) Y_{lm}(\hat{\mathbf{r}}) & \mathbf{r} \in M \end{cases} \tag{18}$$

Here, Ω is the cell volume, and A_{lm} are expansion coefficients. $\mathbf{G}$ denotes a reciprocal lattice vector, and $\mathbf{k}$ is a vector within the first Brillouin zone. Y_{lm} are the spherical harmonics, and u_l is the regular solution of

$$\left[-\frac{1}{2}\frac{d^2}{dr^2} + \frac{l(l+1)}{2r^2} + V(r) - E \right] r u_l(r) = 0 \tag{19}$$

where E is the KS energy of the respective state, and V is the spherical component of the potential in the sphere. A constraint in the APW method is the continuity of the basis functions (18) along the muffin-tin/interstitial boundary. The coefficients A_{lm} are determined by the constraint that the basis functions inside and outside the sphere must be matched.

Consequently, the APW method follows these ideas: Plane waves are solutions to the Schrödinger equation in a constant potential, and in the interstitial region the potential is rather smooth. Also, for the muffin-tin region, the radial functions are solutions to the Schrödinger equation in a spherical potential [31].

4.2 The linearized augmented plane-wave method (LAPW)

As an improvement to the APW method, Andersen linearized the secular problem [32]. This approach, the so-called LAPW method was able to solve some problems inherent to the APW method and enhanced the quality of the computed bandstructures.

Compared to the APW method, the basis functions differ inside the muffin-tin spheres. Looking at the LAPW method, the basis set for the muffin-tin region consists of linear combinations of radial functions, $u_l(r)Y_{lm}(\hat{\mathbf{r}})$ and their derivatives with respect to the energy, but now for a given parameter E_l. The u_l are defined the same way as in Eq. 19. Moreover, the derivative with respect to energy $\dot{u}_l(r)Y_{lm}(\hat{\mathbf{r}})$ satisfies for the non-relativistic case

$$\left[-\frac{1}{2}\frac{d^2}{dr^2} + \frac{l(l+1)}{2r^2} + V(r) - E_l \right] r\dot{u}_l(r) = r u_l(r) \tag{20}$$

The continuity of the functions within the muffin-tins to the values and now also the first derivatives of the plane waves in the interstitial region has to be ensured.

$$\varphi(\mathbf{r}) = \begin{cases} \Omega^{-1/2} e^{i(\mathbf{G}+\mathbf{k})\mathbf{r}} & \mathbf{r} \in I \\ \sum_{lm} [A_{lm} u_l(r) + B_{lm} \dot{u}_l(r)] Y_{lm}(\hat{\mathbf{r}}) & \mathbf{r} \in M \end{cases} \tag{21}$$

Compared to the APW basis expansion (Eq. 18), additional coefficients B_{lm} appear. Just like within the APW scheme, the linear augmented plane waves (LAPWs) are simply plane waves in the interstitial region. The benefit of the LAPW method is the opportunity of treating bands with the same E_l. In most cases, one E_l for all the valence bands is enough; meaning that a single diagonalization is sufficient to get the band energies at a given $\mathbf{k}$-point. In comparison, using only APWs, one diagonalization *for every band* is needed [31].

4.3 The LAPW+LO method

Local orbitals (LO) were introduced by Singh [33] in order to get a better description of semi-core states. Also, LO can accelerate the convergence of the LAPW method via reduction of the required basis set size by improving its flexibility [34]. In this context, local orbitals are added to the LAPW basis set. Here, *local* refers to the fact that they are only non-zero within the muffin-tins.

$$\phi_{l_{lo}}(\mathbf{r}) = \begin{cases} 0 & \mathbf{r} \in I \\ \sum_m [A_{l_{lo}m} u_{l_{lo}}(r) + B_{l_{lo}m} \dot{u}_{l_{lo}}(r) + C_{l_{lo}m} u_{l_{lo}}(r, E_{l_{lo}})] Y_{l_{lo}m}(\hat{\mathbf{r}}) & \mathbf{r} \in M \end{cases} \tag{22}$$

The coefficient $C_{l_{lo}m}$ ensures that $\phi_{l_{lo}}(\mathbf{r})$ becomes zero at the muffin-tin sphere boundaries.

5 Computational details

5.1 Convergence tests and DFT calculations

All calculations in this work are carried out using the full-potential all-electron LAPW+LO package **exciting** [35]. This code features implementations of density-functional theory and many-body perturbation theory including G_0W_0 and the Bethe-Salpeter equation.

As a first step, the unit cell of pristine monolayer MoS_2 is constructed using the experimental value of the lattice constant of 3.1475 Å [36]. For the Kohn-Sham DFT calculations, the GGA-PBE functional [8] is chosen. Next, convergence tests regarding the **k**-grid and the size of the basis set are performed. The muffin-tin radii are set to 2.7 bohr for molybdenum and 1.8 bohr for the sulfur atoms. The smallest radius used, i.e. the 1.8 bohr for the sulfur atoms, implicitly determines the number of basis functions by setting the parameter *rgkmax*. This parameter represents the product of the smallest muffin-tin radius and the maximum length for the $(\mathbf{G}+\mathbf{k})$ vectors. The latter are the basis functions for solving the Kohn-Sham equations. With a fixed parameter $rgkmax = 5.0$, the converged Monkhorst-Pack **k**-grid [37] is determined by paying attention to the total energy obtained for different **k**-grids. From the results in Fig. 3, the total energy is considered as converged for a value of ngridk = 12. This means that a **k**-grid of $12 \times 12 \times 1$ is used for the following DFT calculations. Note, that only one **k**-point in the z-direction is used for calculations of 2D materials.

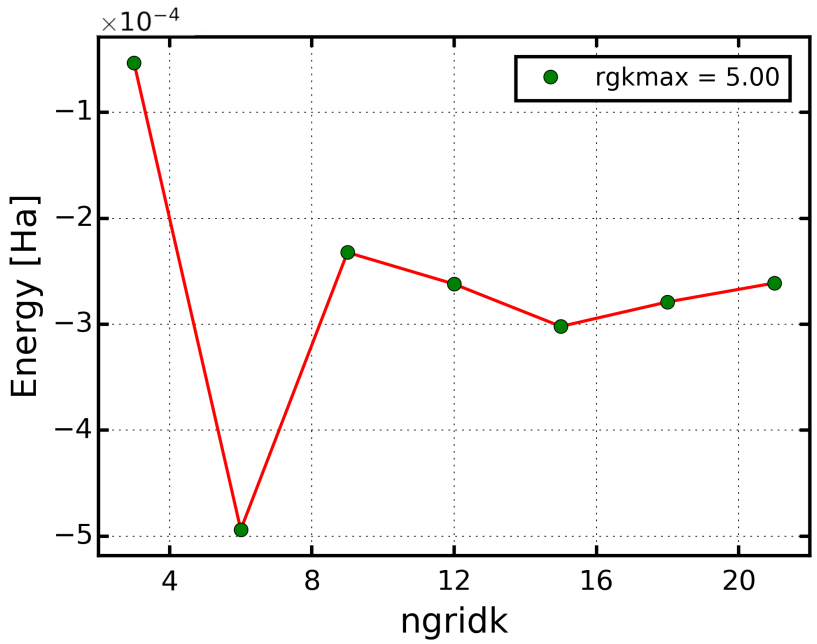

Figure 3: Convergence of the total energy with respect to the parameter *ngridk*. The energy values given on the vertical axis are the deviations from -4848.1030 Hartree. A fixed basis set size parameter rgkmax = 5.0 is used.

Now, with a fixed **k**-grid, the total energy is converged with respect to the parameter rgkmax, and for a value of rgkmax = 6 it is considered as sufficiently converged. This value will be used for the following DFT calculations.

Another important parameter to consider in the convergence tests is the size of the vacuum between adjacent monolayers. Generally it is desirable to have a rather large vacuum for good isolation between the layers, but on the other hand a too large value of the vacuum would lead to increased computing time. Since the bandgap is the property of interest, it is converged with respect to the size of the vacuum. From the results in Fig. 4, a vacuum of 30 bohr is found to be sufficient.

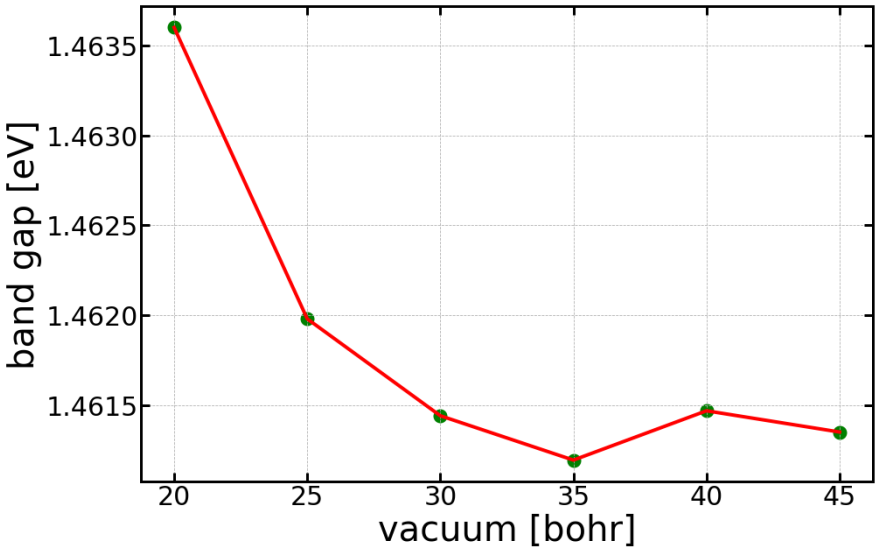

Figure 4: Convergence of the band gap with respect to the vacuum in the out-of-plane direction.

5.2 G_0W_0 calculations

For the G_0W_0 calculations, the vacuum is extended to 38 bohr. Also, a truncated Coulomb potential in the z-direction is applied, meaning that it gets a value of zero before reaching the adjacent monolayers. A very dense **k**-grid is required for 2D semiconductors because the dielectric function $\varepsilon(q)$ is very strongly dependent on q, especially for $q \to 0$. The use of a dense **k**-grid means the need of very large memory, where even state-of-the-art computer clusters reach their limits. This makes the calculations very hard to converge.

Rasmussen and co-workers [38] proposed a strategy to converge the G_0W_0 eigenvalues even with the use of a coarser **k**-grid. For a coarser **k**-grid, the quasiparticle energies differ from the converged ones, using a very fine **k**-grid, by approximately a rigid shift. It is suggested to use a **k**-grid of $30 \times 30 \times 1$ for the DFT calculations which are the base for the G_0W_0 correction. Following this plan, first the impact of the included empty states, that are used for constructing the screened Coulomb interaction and the self energy, is checked. With this in mind, convergence is tested with respect to the parameter defining the included number of empty states. Then, a G_0W_0 calculation on a rather coarse **k**-grid of $12 \times 12 \times 1$ (where bandgap value I is obtained) and one on a fine **k**-grid of $30 \times 30 \times 1$ (where bandgap value II is obtained) is performed, both with the same (rather small) number of empty states. Afterwards, another

calculation with the *converged* value of empty states is performed just on the coarse **k**-grid of $12 \times 12 \times 1$ (where bandgap value III is obtained). The converged value of the bandgap can then be extrapolated by calculating $III - (I - II)$. It was shown by Rasmussen et al. that an even finer **k**-grid of $45 \times 45 \times 1$ just induces a change to the fundamental bandgap by less than 0.1 eV, meaning that a **k**-grid of $30 \times 30 \times 1$ can be considered to give rise to a sufficiently converged bandgap value for the present problem.

5.3 BSE calculations

The solution of the Bethe-Salpeter equation gives information about the electron-hole interaction, and furthermore gives rise to the macroscopic transverse dielectric tensor. In the case of monolayer MoS_2 - because of its hexagonal crystal system - this tensor has only non-zero diagonal elements, where the xx- and yy-components are the same. The aim is to calculate the imaginary part of these in-plane components in order to get access to the optical absorption spectrum of the monolayer.

As a first step, careful convergence tests are made for the pristine unit cell. A k/q-grid of $12 \times 12 \times 1$ is found to be sufficient with respect to the dielectric function. The regular k-mesh (containing the Γ point) is shifted by a small displacement in all three directions so that all the **k**-points are now crystallographically inequivalent [39]. Also, 30 empty states are found to be sufficient for the calculation, and a Lorentzian broadening of 0.004 Hartree is used. It is found sufficient to include 3 valence and 3 conduction bands in the calculation for evaluating the transitions that give rise to the excitons near the band gap. The DFT-BSE approach is used, including a scissors operator of 0.88 eV, which is the difference between the *GW* and the KS band gap. This means that as a starting point for the BSE calculations, the DFT eigenvalues are used, but the band gap is widened by 0.88 eV because of its well-known underestimation by DFT [40]. Because of bands folding back into the first Brillouin zone, for the bigger supercells containing sulfur vacancies, more valence and conduction bands have to be included in order to consider the same energy ranges. Therefore, for the 12.50 %-SV-MoS_2, 10 valence and conduction bands each are included and for the 5.56 %-SV-MoS_2, 25 each are taken into account. Because there is vacuum in the z-direction of the unit cell, the volume considered for the dielectric function is rescaled by [41]

$$V_{eff} = \frac{a_{eff}}{a_z} * V \tag{23}$$

where a_{eff} is the material thickness (11.62 bohr) and $a_z = a_{eff} + a_{vac}$. The vacuum included in the calculation is $a_{vac} = 38$ bohr.

6 Results

In this chapter, the results for pristine monolayer MoS_2 and for SV-MoS_2 with two different vacancy concentrations are presented. This includes structural properties, charge-density distribution, bandstructure, and projected density of states as well as the optoelectronic properties including absorption spectrum and analysis of the excitons.

6.1 Structural properties

With the aim of studying sulfur vacancies, a 2×2 and a 3×3 supercell are built, and one sulfur atom is taken out of each of the cells. This results in a sulfur vacancy concentration of 12.50 % for the 2×2 supercell and 5.56 % for the 3×3 supercell. Then, the lattice constant of these cells has to be optimized and the atom positions need to be relaxed, i.e. there should be no force on the atoms. The lattice constants leading to the least total energy are the natural ones. For the two supercells containing vacancies, the difference of the total energy to its minimum value with respect to different lattice constants can be seen in Fig. 5. Optimized lattice constants of 3.12 Å for the case of 12.50 % vacancy concentration and 3.16 Å for the cell with 5.56 % vacancy concentration are obtained. The relaxed lattice constant of 3.19 Å for *pristine* MoS_2 obtained with the GGA-PBE functional is larger than the experimental value as reported by Young (3.1475 Å) [36].

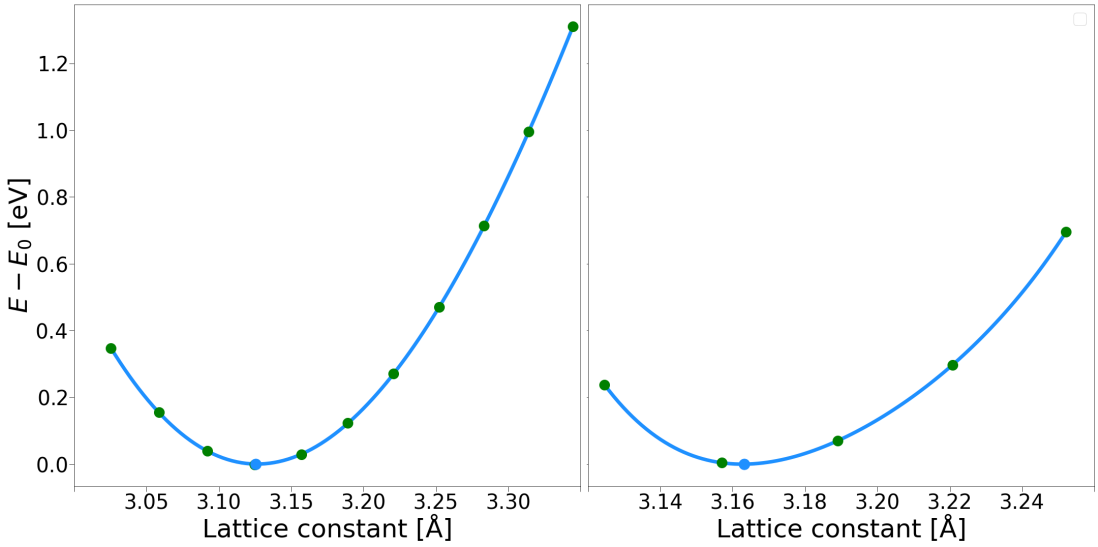

Figure 5: Difference of the total energy E to its minimum value E_0 with respect to the lattice constant used in the Kohn-Sham calculations for the 2×2 cell (left) and 3×3 cell (right). The minimum of the fitted curve is indicated by a light blue dot. A polynomial fit of order 4 is used.

In Table 1, the lattice parameters and the bondlengths of 12.50 %-SV-MoS_2 and 5.56 %-SV-MoS_2 are compared to those of the pristine material. For the 2×2 and 3×3 supercells, the lattice parameters are divided by two and three, respectively, in order to compare with the pristine cell. The given Mo - S bondlengths are averaged. A tendency to a decrease of the bondlengths and the lattice parameter is observed, resulting from the SVs. As expected, the lower the vacancy concentration, the closer are the values to those of the pristine material. The bondlengths between molybdenum and sulfur atoms are shown in Fig. 6 for exemplary cases of atoms close to a vacancy and atoms that are farther away from it. The sulfur atoms considered

in the figure are in the opposite sulfur plane to the vacancy, which is marked as a red dot in the figure. On top of the vacancy there is also a sulfur atom. Sulfur vacancies make Mo and S atoms bind more tightly and the Mo - S bondlength gets smaller, the closer the atoms are to the vacancy.

Table 1: Lattice parameters and averaged bondlengths (given in Å) of pristine MoS_2, 5.56 %-SV-MoS_2 and 12.50 %-SV-MoS_2. For comparison, the lattice parameters of the 2×2 and 3×3 supercells are divided by two and three, respectively.

Lattice parameters and averaged bondlengths in Å		
S vacancy concentration	**lattice parameter**	**Mo - S**
pristine	3.19	2.42
5.56 %	3.16	2.41
12.50 %	3.12	2.40

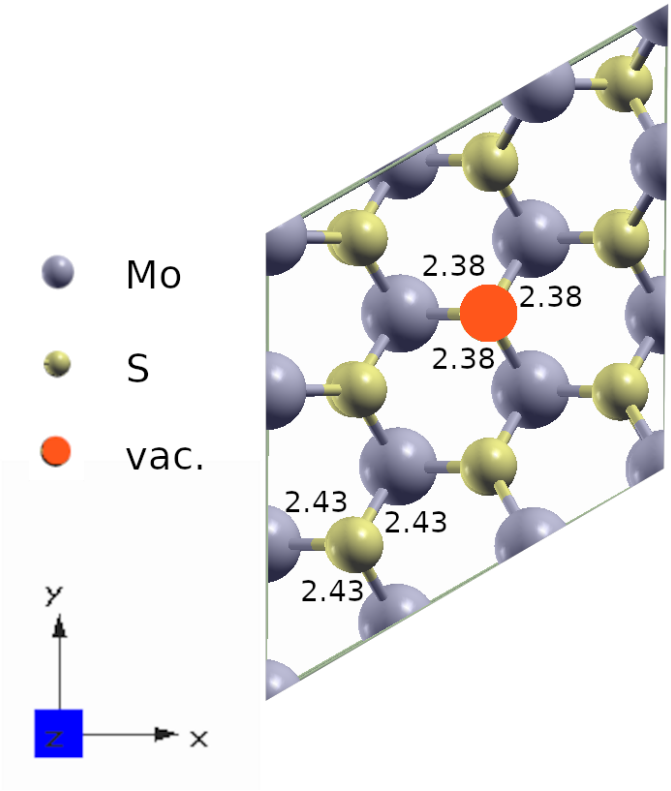

Figure 6: The bondlengths in Ångstrom between exemplary Mo and S atoms. The considered sulfur atoms are chosen in the plane that contains sulfur atoms opposite to the vacancy. The sulfur vacancy is marked with a red dot, that symbolises that the vacancy is behind a sulfur atom.

6.2 Charge density distribution

The charge density distribution in the xz-plane of the pristine material is compared to that of a sulfur vacancy cell in order to get a better understanding of the decrease of the Mo-S bondlength around the vacancies.

The following plot (Fig. 7) compares the charge density distribution of the pristine material (upper panel) to that of 12.50 %-SV-MoS_2 (lower panel), looking at the xz-plane. For the pristine case, the molybdenum atoms can be seen between the pairs of opposing sulfur atoms. The sulfur vacancy is clearly visible in the lower panel. It is marked by a black square. It can be seen that the charge arising from the molybdenum atoms tends to spread more in space, reaching out more to the sulfur layers, compared to the upper panel. Consequently, the charge distribution in the vicinity of the vacancy differs characteristically from the pristine one.

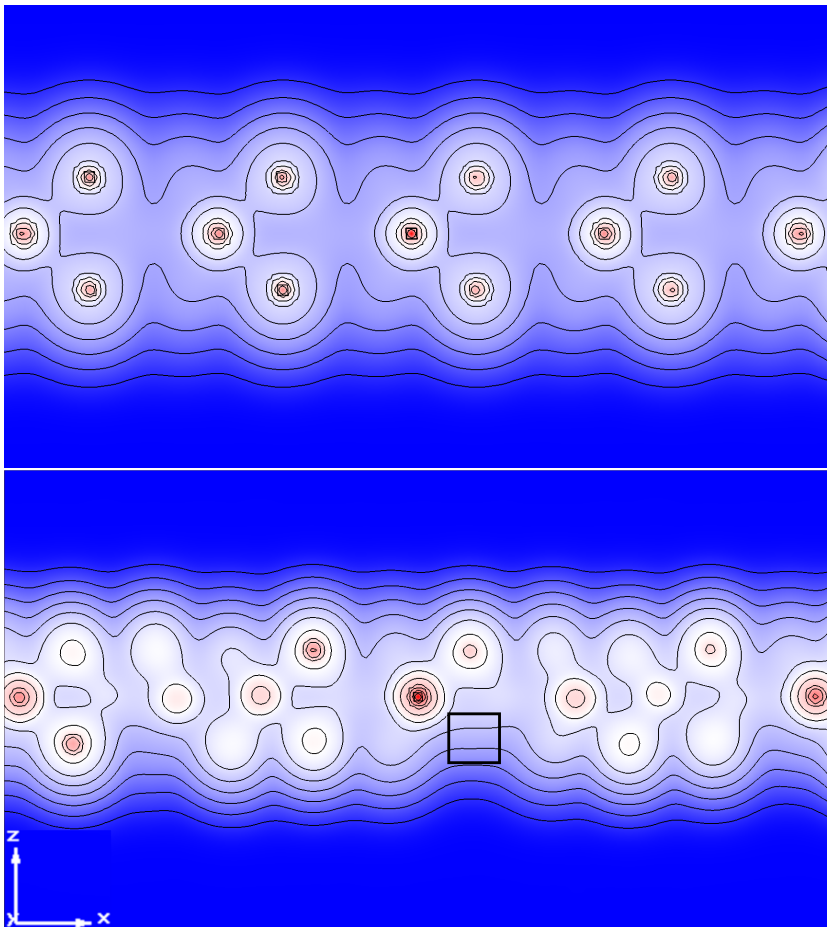

Figure 7: Charge density distribution in the xz-plane of pristine MoS_2 (top) and 12.50 %-SV-MoS_2 (bottom), where red indicates a high charge density and blue one of zero value. The vacancy is indicated by the black square.

A closer look on the difference in charge density between pristine MoS_2 and 12.50 %-SV-MoS_2 is given in Fig. 8. The sulfur vacancy (indicated as *vac.*) can be seen as a big red spot, which means a decrease in the charge density compared to the pristine case. Blue areas indicate an increase in charge density for the vacancy case, while green areas show no charge

density difference. The molybdenum atom in the vicinity of the vacancy reacts by shifting its charge density closer to both the vacancy and the sulfur atom opposite to it. As a consequence, also the sulfur atom moves a bit farther away from the vacancy. All in all, this charge density redistribution due to the vacancy leads to the decrease in the Mo-S bondlength around the vacancy because the Mo atom gets closer to the S atom.

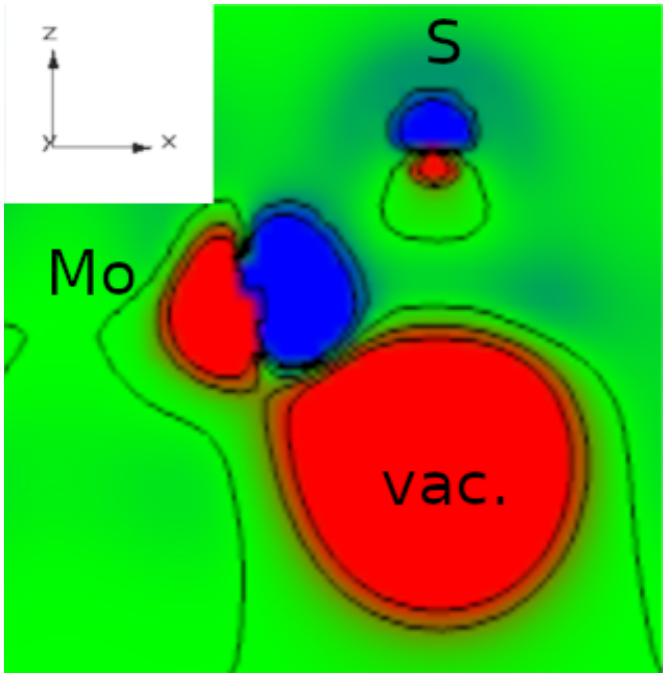

Figure 8: Difference in the charge density distribution between pristine MoS_2 and 12.50 %-SV-MoS_2 in the xz-plane. Red means a decrease in charge density for the vacancy cell compared to the pristine one, while blue indicates an increase. Green areas show no charge density difference.

6.3 Electronic structure

The Kohn-Sham bandstructures as well as the corresponding projected densities of states (PDOS) of the sulfur vacancy cells are examined in this section. Furthermore, the G_0W_0 bandstructures are presented.

6.3.1 Kohn-Sham bandstructure

In the following, the Kohn-Sham bandstructures as well as the corresponding densities of states are presented. The parameters as described in chapter 5 are used. Of course, the **k**-grid is adjusted to the supercells, i.e. for the 1×1 cell a **k**-grid of $12 \times 12 \times 1$ is used, and for the 2×2 cell it is a $6 \times 6 \times 1$ **k**-grid due to the reciprocal length scale. For the 3×3 cell, also a **k**-grid of $6 \times 6 \times 1$ is used because the **k**-points in the x- and y-direction should be multiples of 2 and 3 in order to guarantee the inclusion of the high-symmetry points M and K. The path as shown in Fig. 9 (a) is used for plotting the bandstructures.

First, the KS bandstructure of pristine monolayer MoS_2 is obtained (Fig. 9 (b)), exhibiting a direct Kohn-Sham bandgap of 1.79 eV at K. This bandgap value corresponds to a wavelength of

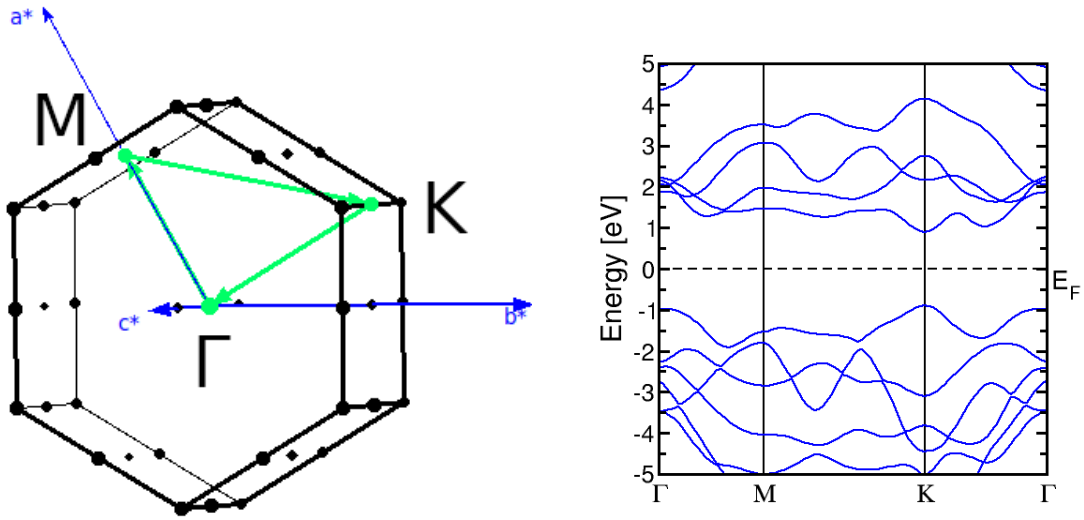

(a) (b)

Figure 9: (a) First Brillouin zone, showing the path along the high-symmetry points Γ, M, and K, as well as the primitive reciprocal lattice vectors. (b) Kohn-Sham bandstructure of monolayer MoS_2 with its direct bandgap of 1.79 eV at K.

693 nm, that is in the visible spectrum. Here it should be noted that the Kohn-Sham bandgap is usually underestimated. Interestingly, its value of 1.79 eV coincides with the *optical* bandgap that was found experimentally [4]. This is because of a cancellation effect in the present case, as the quasi-particle correction is approximately equal to the highest absolute exciton binding energy. The optical bandgap is lower than the electronic bandgap because it also considers these excitonic features. Further analysis of the electronic structure using the projected density of states (Fig. 10) reveals that bands around the Fermi level mainly arise from molybdenum d-orbitals. The narrow overlap of d-orbitals is the reason why the bands around the Fermi level, as shown in Fig. 9 (b), appear to be rather flat.

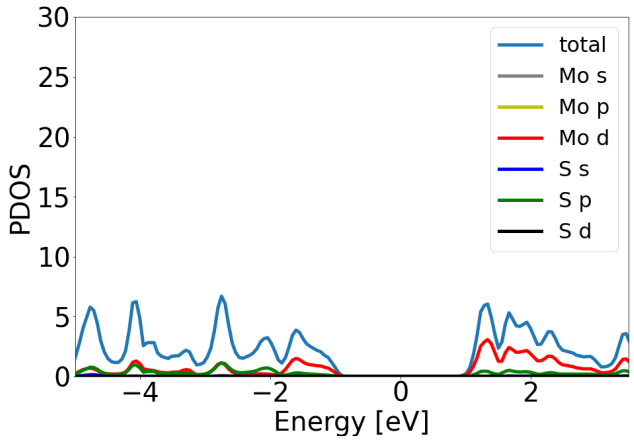

Figure 10: Projected density of states (PDOS) in $states/(eV * unit\,cell)$ of the pristine MoS_2 cell. Most contributions to the bands arise from Mo d-orbitals, followed by S p-orbitals.

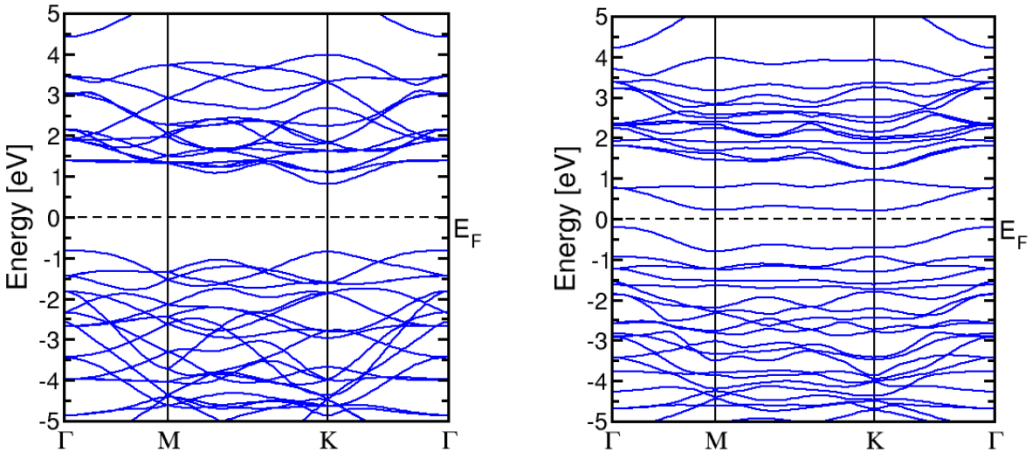

(a)

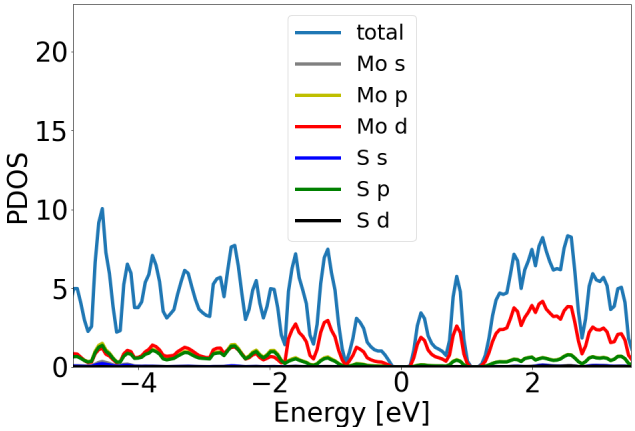

(b)

Figure 11: (a) Comparison of the Kohn-Sham bandstructures of 2×2 supercells of pristine MoS_2 and 12.50 %-SV-MoS_2. (b) PDOS in $states/(eV * unit\,cell)$ of the 12.50 %-SV-MoS_2 cell.

Next, the bandstructure of the 2×2 cell with sulfur vacancies is shown. In order to compare the obtained bandstructure easier with the one of the pristine MoS_2, the latter is calculated again, but this time also on a 2×2 cell (Fig. 11 (a) left side). The bands fold back into the first Brillouin zone of the supercell, that is smaller than the one corresponding to the 1×1 cell. For hexagonal symmetry, a simple 3N-rule [42] is valid: for a $(3N-1) \times (3N-1)$ supercell, the K point of the primitive cell folds to the K point of the supercell, while for a $(3N) \times (3N)$ supercell the K point of the primitive cell folds to Γ of the supercell. Here, N denotes any integer number. That is why the pristine 2×2 cell indeed shows a direct bandgap at K, as it is also the case for the 1×1 cell. In Fig. 11 (a) right side, the formation of additional defect-related states in the bandstructure of SV-MoS_2 is obvious. Thereby, the fundamental bandgap decreases drastically to 0.41 eV compared to 1.79 eV for the pristine material. Also, the bandgap becomes indirect, from Γ to K (the high-symmetry points are given in the supercell's first Brillouin zone). From the projected density of states (Fig. 11 (b)) it can be seen that there is much impact of the Mo d-orbitals on the defect-related states. Further investigation of the bandstructure's character

shows the origin of the observed defect-related states: d-orbitals of molybdenum atoms that are located directly next to sulfur vacancies account for these defect-related states. Looking at the contributions of molybdenum atoms that are *not* located directly next to a sulfur vacancy shows that these atoms only contribute to bands that are also there in the pristine bandstructure.

Going further, the impact of spin-orbit coupling on the bandstructure is investigated. It turns out, that the splitting of the bands remains small and therefore has no large effect on the fundamental bandgap, as can be seen in Fig. 12. The bandgap decreases only insignificantly from 0.41 eV to 0.38 eV. With this in mind and for the sake of reasonable computational costs, spin-orbit coupling will be neglected later on in the BSE calculations.

Turning to the 3×3 supercell, with a vacancy concentration of 5.56 %, the isolated defect-related states are energetically more localized compared to the cell with the higher vacancy concentration, as can be seen from the bandstructure and the density of states (Figs. 12 and 13). More detailed, these states spread over a range of 0.97 eV for the 2×2 cell, while for the 3×3 cell it is a range of only 0.44 eV. This difference arises from the fact that the defects are closer to each other in the case of the 2×2 cell, which leads to more overlap of the defect states and therefore a stronger dispersion in the bands. It can be extracted from Figs. 11 (b) and 13, that the predominant contribution to the electronic bands stems from molybdenum d-orbitals. Also, there is a small contribution arising from sulfur p-orbitals around the bandgap, that becomes more significant farther away from the Fermi level. As expected, the bandgap of 0.86 eV, corresponding to the 3×3 cell, is not as small as for the high vacancy concentration 2×2 cell, as can be seen in Fig. 12. Following the 3N-rule [42], the K point of the pristine cell folds to the Γ point of the 3×3 supercell. The bandgap is direct, from Γ to Γ in the supercell's first Brillouin zone.

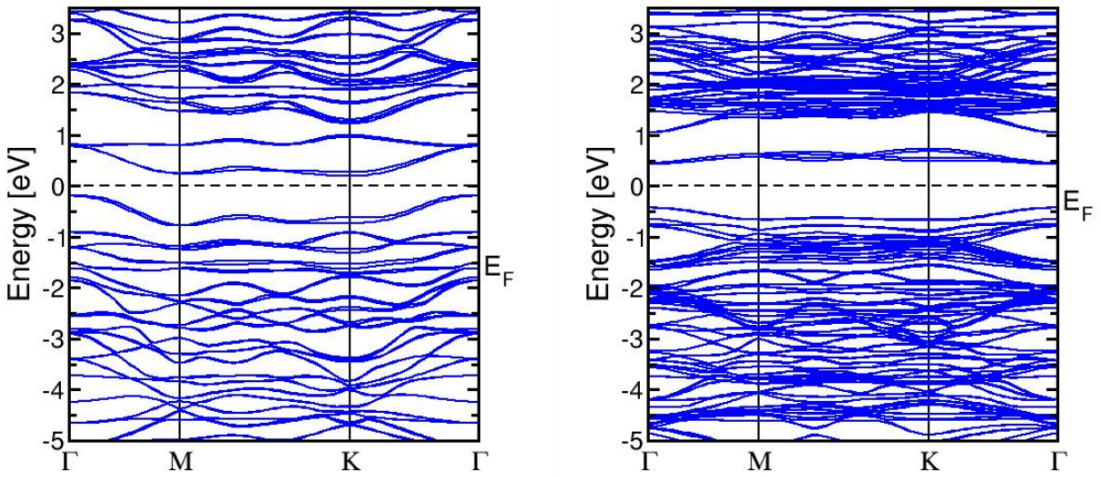

Figure 12: Comparison of the KS bandstructures of the two MoS_2 cells with different vacancy concentrations. Spin-orbit coupling is included. Left: concentration of 12.50 %, bandgap of 0.38 eV. Right: concentration of 5.56 %, bandgap of 0.86 eV.

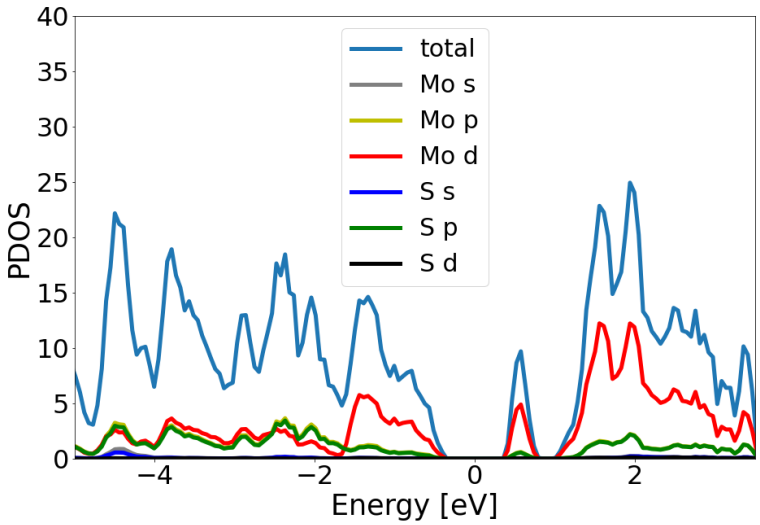

Figure 13: Projected density of states (PDOS) in $states/(eV * unit\,cell)$ of the 5.56 %-SV-MoS_2 cell.

6.3.2 G_0W_0 bandstructure

In this section, the G_0W_0 bandstructures of pristine MoS_2 and SV-MoS_2 with two different vacancy concentrations are presented. For 2D semiconductors, the G_0W_0 calculations usually demand a very fine **k**-grid, which is computationally costly. Therefore a more efficient convergence strategy following Rasmussen [38] is employed (see also section 5.2). Two G_0W_0 calculations for pristine MoS_2 are performed, both with 50 empty states included, but with **k**-grids of $12\times12\times1$ and $30\times30\times1$, respectively. The bandstructures for both cases are compared in Fig. 14. It can be seen that the conduction bands of the case with the $12 \times 12 \times 1$ **k**-grid are shifted to higher energies, while the valence bands are shifted to lower energies, compared to the bands corresponding to the $30 \times 30 \times 1$ grid. As an approximation, the bandstructure related to the finer grid can be considered as the one related to the coarser grid, corrected by a narrowing of the bandgap. Therefore, in order to keep computation time reasonable, the G_0W_0 calculations for the supercells are performed on **k**-grids corresponding to $12 \times 12 \times 1$ for the case of the 1×1 cell. Then, the bandgap is corrected by narrowing it by the difference of the bandgaps in Fig. 14, which is 0.39 eV.

Something noteworthy appears in the G_0W_0 bandstructure of the pristine case, as can also be seen from Fig. 14: using the **k**-grid of $30 \times 30 \times 1$, it shows an indirect bandgap of 2.67 eV, although the bandgap of monolayer MoS_2 is well known to be direct. This happens, because in this calculation, the experimental value of the lattice constant is used. Hüser et al. examined this phenomenon and stated: "[...] we conclude that the G_0W_0@LDA band gap of monolayer MoS_2 is indirect with a value of 2.6 eV while the direct gap is 2.8 eV, when the experimental lattice constant of 3.16 Å is used. [...] self-consistent GW calculations have been shown to consistently yield direct band gaps of 2.75–2.80 eV." [43, 44, 45]

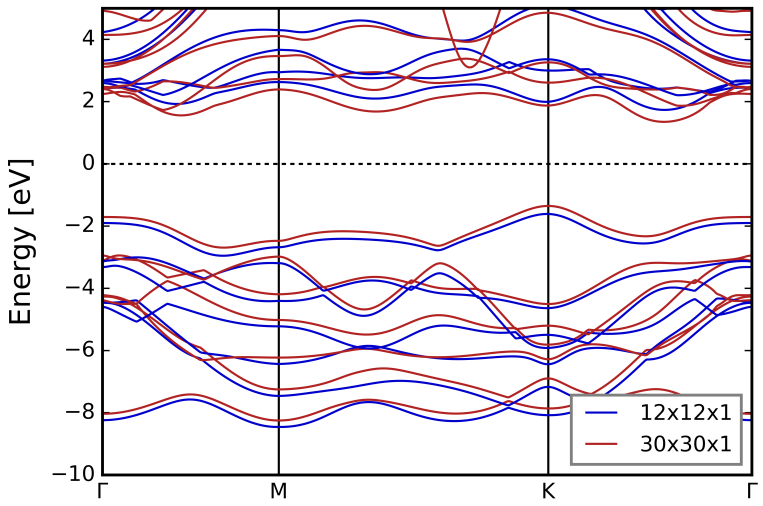

Figure 14: G_0W_0 bandstructures of pristine monolayer MoS_2 with **k**-grids of $12\times12\times1$ (blue) and $30\times30\times1$ (red), respectively. 50 empty states are used in both calculations. The difference between the two G_0W_0 bandstructures is approximately a narrowing of the bandgap from the coarser grid to the finer one. A difference in the bandgap's value of 0.39 eV is observed.

Fig. 15 shows the G_0W_0 bandstructures of 12.50 %-SV-MoS_2 and 5.56 %-SV-MoS_2, respectively. It is important to include a number of **k**-points in the x- and y- directions, which is a multiple of 3 and 2, in order to include the high-symmetry points K and M properly. Therefore both bandstructures are obtained from calculations on a $6 \times 6 \times 1$ **k**-grid. As discussed, the resulting band gaps are over-estimated and thus, the values using a correction of -0.39 eV, are given. For 12.50 %-SV-MoS_2 in particular, the defect-related states entangle with the conduction bands and are no longer isolated, as they were in the Kohn-Sham bandstructure. A rather strong band dispersion is observed for the material with higher vacancy concentration. 12.50 %-SV-MoS_2 turns out to have an indirect quasiparticle bandgap of 1.73 eV. On the other hand, for the lower sulfur vacancy concentration (5.56 %), the defect-related states are still isolated, like in the Kohn-Sham bandstructure. Compared to 12.50 %-SV-MoS_2, the band dispersion is not as distinct. The bandstructure reveals an indirect quasiparticle bandgap of 2.28 eV. It should be noted that, for the sake of lower computational costs, the G_0W_0 correction was only calculated for conduction bands ranging up to approximately 3.2 eV above the Fermi level. This is why above this energy, the bands are not shown in the right plot of Fig. 15.

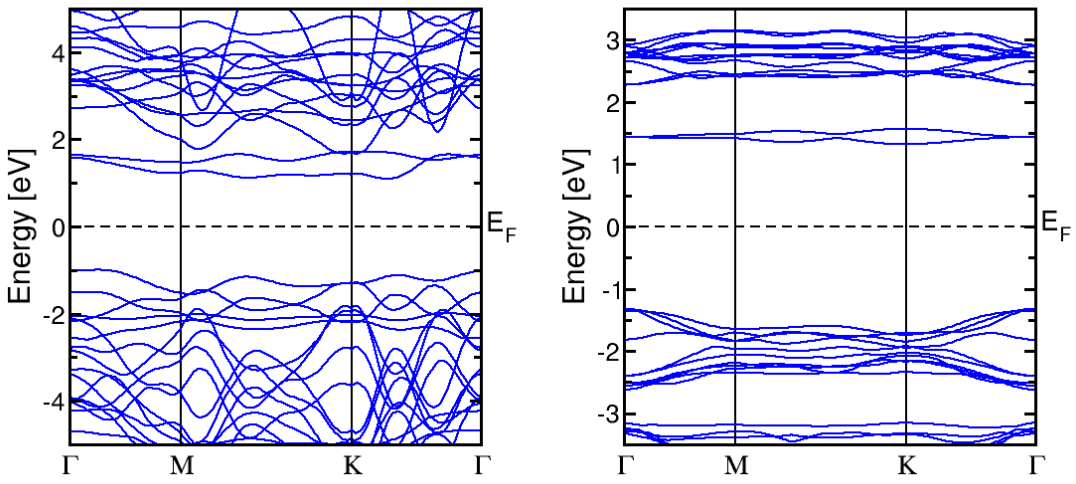

Figure 15: Left: 12.50 %-SV-MoS_2: G_0W_0 bandstructure as obtained by using a $6 \times 6 \times 1$ **k**-grid. After applying a correction of -0.39 eV, the value of the bandgap is 1.73 eV. Right: 5.56 %-SV-MoS_2: G_0W_0 bandstructure as obtained by using a $6 \times 6 \times 1$ **k**-grid. After applying a correction of -0.39 eV, the value of the bandgap is 2.28 eV.

6.4 Optical properties

In this chapter, the main focus is on the absorption spectra, as obtained by BSE calculations. Then, the excitons are analyzed, in reciprocal space as well as in real space.

6.4.1 Absorption spectra

As a first step, the absorption spectrum of the pristine material is calculated using the DFT-BSE approach. Thereby, the DFT bandgap is widened by 0.88 eV in order to mimic the G_0W_0 bandgap of 2.67 eV. The full BSE Hamiltonian is diagonalized, as the singlet states are computed. Then the imaginary part of the in-plane dielectric function, that corresponds to the absorption spectrum, is calculated. The obtained dielectric function is rescaled, in order to account for the vacuum that is included in the unit cell volume. By comparing the result (blue curve in the *BSE singlet* plot in Fig. 16) to already published work [46], it turns out that there is good agreement to it. Following the literature, the significant excitonic peaks of pristine MoS_2 are labelled as A and B, respectively [46, 4]. A slight blueshift of the entire spectrum compared to the literature values is likely to be caused by the fact, that there is no spin-orbit coupling included in the calculations in the present work. Rasmussen et al. state, that the inclusion of spin-orbit coupling decreases the bandgap of pristine MoS_2 by 0.17 eV [38].

Also for the vacancy cells, the DFT bandgap is widened by 0.88 eV. The BSE results regarding SV-MoS_2 show that sulfur vacancies tend to redshift the absorption spectrum and to decrease its maximum intensity. The maximum intensity of 5.56 %-SV-MoS_2 is still approximately 2/3 of the pristine value, but for 12.50 %-SV-MoS_2 it is not even half of it. This can be extracted from the *BSE singlet* plot in Fig. 16. Surprisingly, the absorption onset of the 5.56 % vacancy concentration is at lower energies than that of the higher vacancy concentration case. The reason for this is further examined by calculating the joint density of states (JDOS):

$$JDOS(\hbar\omega) = \frac{2}{8\pi^3} \int \delta[E_c(\mathbf{k}) - E_v(\mathbf{k}) - \hbar\omega]\, d^3k \tag{24}$$

This is an expression for the number of states per unit volume and unit energy range, that occur with an energy difference between the valence and conduction bands that is equal to the photon energy $\hbar\omega$ [27]. The imaginary part of the dielectric function can be considered proportional to $\frac{JDOS}{E^2}$ [47]. Of course, this approximation of $\Im\,\epsilon_M$ does not consider any excitonic features, as the BSE singlet calculation does. The plot of $\frac{JDOS}{E^2}$ reveals that the onset of the spectrum increases in energy from the highest to zero vacancy concentration. For a more sophisticated analysis of $\Im\,\epsilon_M$, the BSE equation is solved in the Independent Particle Approximation. This means that only the diagonal part of the BSE Hamiltonian is considered. Again, as also for the approach using the JDOS, it can be clearly seen, that the onset energies increase from highest to zero vacancy concentration. It can therefore be concluded, that the peculiarity of the lowest absorption onset for the 5.56 %-SV-MoS_2 is an excitonic feature, because it appears only when the full BSE singlet Hamiltonian is taken into account. A lower vacancy concentration leads in the present case to stronger bound excitons. While the lowest exciton binding energy for 12.50 %-SV-MoS_2 is -0.48 eV, it is -0.58 eV for the 5.56 % vacancy concentration case (exciton C).

The Independent Particle Approximation (IPA) pronounces several absorption peaks more than the approach using the JDOS. Looking at the blue curve for the pristine material, the absorption onset at the bandgap of 2.67 eV is clearly visible in the IPA spectrum, leading to a peak around 2.95 eV. This peak is hardly visible in the JDOS spectrum, while in the BSE singlet spectrum, this peak is in fact the highest in the whole spectrum. The peak around 3.70 eV, which is the highest using only the IPA is not so pronounced in the BSE singlet spectrum. Of course, the excitonic peaks at 2.31 eV (exciton A) and at 2.51 eV (exciton B) are only

present in the BSE singlet spectrum, because the exchange term as well as the direct term considering electron-hole pairs are taken into account there. The orange curve corresponding to 5.56 % SV-MoS_2 shows the onset at the bandgap of 1.73 eV in the JDOS approach. Peaks are observed around 2.10 eV and 2.70 eV using the JDOS and the IPA approach. Beyond 3 eV, absorption is steadily increasing, while in the BSE singlet spectrum, the overall peak is reached already at 2.75 eV. For 12.50 % SV-MoS_2 (green curve) the onset appears at the bandgap of 1.25 eV in the IPA spectrum, while this is not clearly visible in the JDOS approach. There are peaks around 1.80 eV, 2.35 eV and 3 eV in the JDOS as well as in the IPA spectra. The BSE singlet approach shifts the onset to slightly lower energies due to bound excitons. The global peak in the calculated range of the imaginary part of the dielectric function is at 3.50 eV.

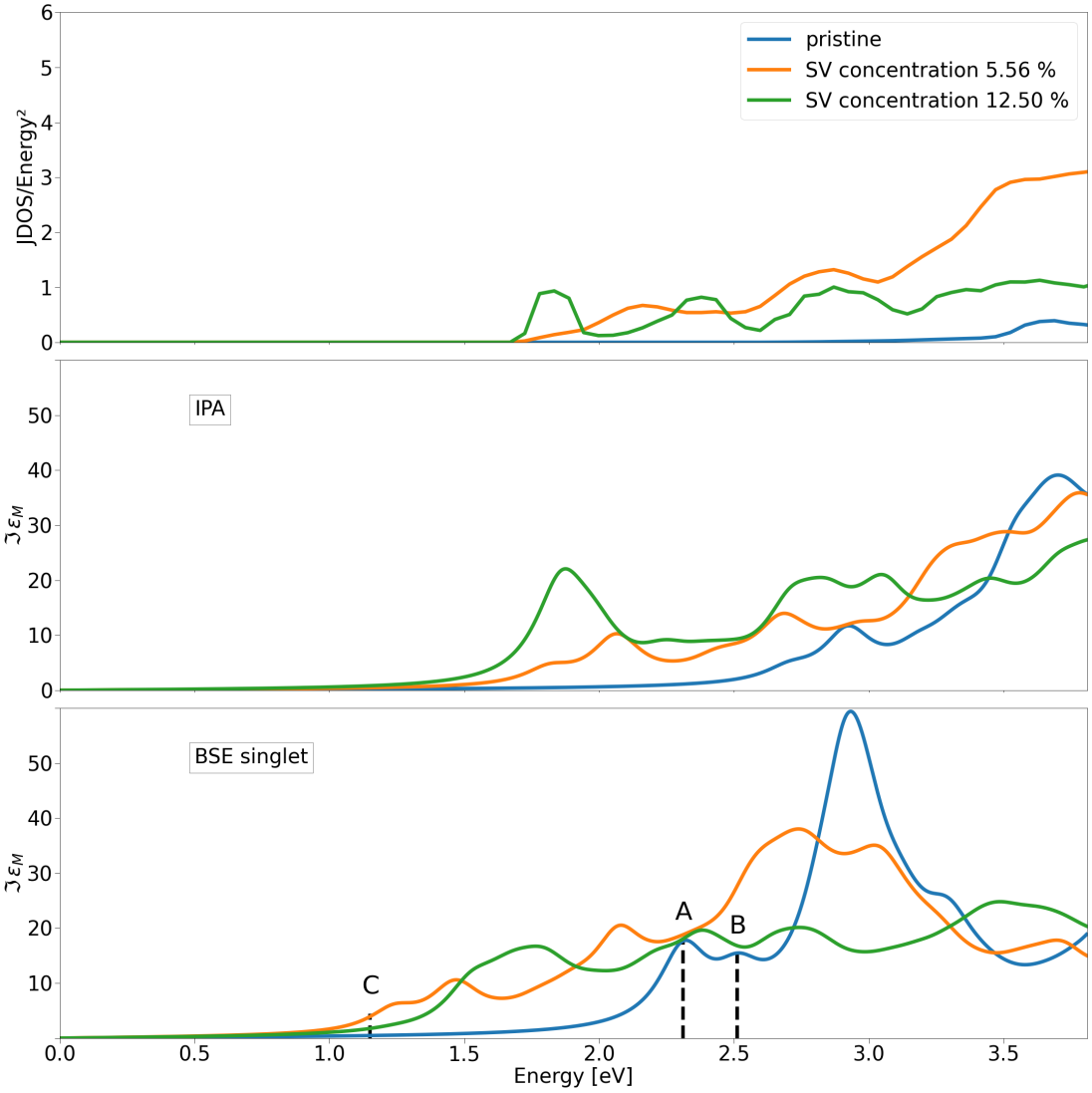

Figure 16: $JDOS/Energy^2$ and imaginary part of the in-plane dielectric function of pristine MoS_2 (blue), 5.56 %-SV-MoS_2 (orange) and 12.50 %-SV-MoS_2 (green); as obtained from the Independent Particle Approximation (IPA) and BSE singlet calculations. A Lorentzian broadening of 0.11 eV is used. Significant excitonic features are labeled A and B, and C.

6.4.2 Exciton wavefunctions in reciprocal and real space

This section is dedicated to analyzing the significant excitonic features labeled A, B, and C in the obtained BSE spectra. Therefore the excitons are examined in reciprocal and real space. Figs. 17 (a) and 18 (a) show the excitonic weights corresponding to the excitons A and B, respectively, projected onto the Kohn-Sham bandstructure of pristine MoS_2. Both excitons have their weights localized around the K point, at the valence band maximum and conduction band minimum. The exciton wavefunction is non-periodic. Therefore, for its meaningful visualisation in real space it is necessary to use supercells. $3 \times 3 \times 1$ supercells are adopted in the present case. Figs. 17 (b) and 18 (b) show probability density isosurfaces for the electron part of excitons A and B, respectively. They are plotted in blue, using an isovalue of approximately 3 % of the maximum value of the probability density. In the figures, the position of the hole is fixed close to the unit cell's origin in order to reduce the wavefunction's dimensionality from six to three dimensions. The hole's position is marked with a black dot. For a fixed hole at the Mo atom in the origin, the electron orbitals of exciton A in Fig. 17 spread around Mo atoms distributed over the whole $3 \times 3 \times 1$ cell. For the case of exciton B in Fig. 18, the probability density of the electron part of the exciton wavefunction is found to be high especially around the Mo atoms that build a hexagon around the hole's position. In neither of the two examined excitons is the electron wavefunction located around sulfur atoms.

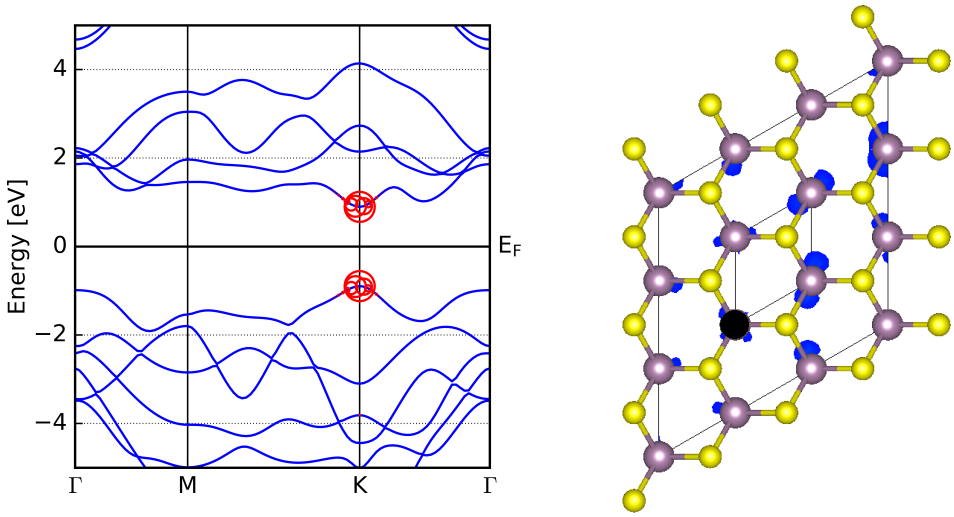

(a) (b)

Figure 17: Pristine MoS_2: (a) Excitonic weights of exciton A (binding energy of -0.36 eV) projected onto the bandstructure, shown as red circles. (b) Probability density isosurface (blue) of the electron part of exciton A. The hole is fixed near the Mo atom located at the black dot.

The cells containing sulfur vacancies show behaviour similar to the pristine case in terms of the localization of the excitons in reciprocal space. Fig. 19 (a) shows the projection of the excitonic weights of exciton C onto the bandstructure of the 5.56 % vacancy case. Exciton C has the lowest binding energy overall, it is -0.58 eV. Its excitonic weights are projected mainly onto the Γ point, which corresponds to the K point of a 1×1 unit cell. This exciton is responsible that the onset of the imaginary part of the dielectric function appears at lower energies than the onset corresponding to the 12.50 % vacancy case.

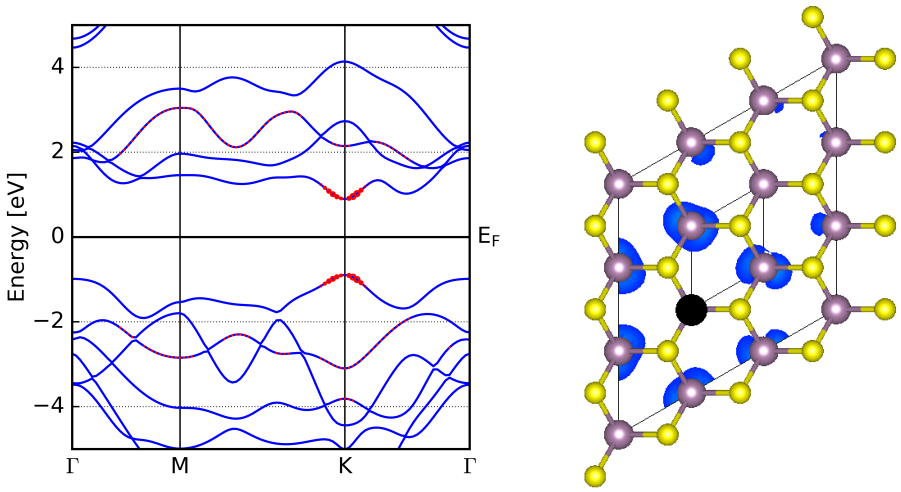

(a) (b)

Figure 18: Pristine MoS_2: (a) Excitonic weights of exciton *B* (binding energy of -0.16 eV) projected onto the bandstructure, shown as red circles. (b) Probability density isosurface (blue) of the electron part of exciton *B*. The hole is fixed near the Mo atom located at the black dot.

Fig. 19 b) shows probability density isosurfaces of the electron part of exciton *C*. An interesting finding is the fact that the electron wavefunction is localized around molybdenum atoms next to sulfur vacancies (marked as red dots).

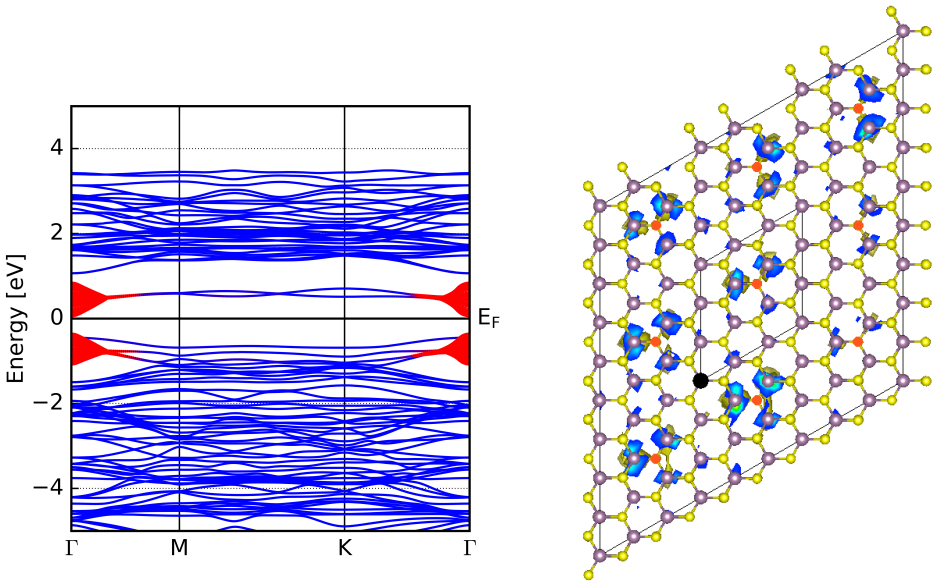

(a) (b)

Figure 19: 5.56 %-SV-MoS_2: (a) Excitonic weights of exciton *C* (binding energy of -0.58 eV) projected onto the bandstructure, shown as red circles. (b) Probability density isosurface (blue) of the electron part of exciton *C*.

7 Summary

This work has been dedicated to study theoretically the impact of sulfur vacancies (SV) on the optoelectronic properties of monolayer molybdenum disulfide (MoS_2). With this goal in mind, *ab initio* calculations have been performed, including density-functional theory, G_0W_0, and the Bethe-Salpeter equation (BSE).

A decrease of the Mo-S bondlength in SV-MoS_2 compared to pristine MoS_2 has been found. Regarding the bandstructures of the SV-MoS_2 samples, defect-related states have appeared, decreasing the fundamental bandgap drastically compared to pristine MoS_2. Consequently, it has been observed, that SVs tend to redshift the absorption spectrum and decrease its maximum intensity in the computed range up to 3.8 eV. An analysis of the excitons has shown rather localized excitonic weights in reciprocal space and a spread of the wavefunctions over several unit cells in real space. When the hole has been fixed near an Mo atom, the electron's wavefunction has been seen to be localized around Mo atoms which are situated directly next to a sulfur vacancy.

References

[1] B. Radisavljevic, A. Radenovic, J. Brivio, V. Giacometti, A. Kis. *Single-layer MoS_2 transistors.* Nature nanotechnology **6** (2011) 147.
doi:10.1038/nnano.2010.279

[2] M.-l. Tsai, S.-H. Su, J.-K. Chang, D.-S. Tsai, C.-H. Chen, C.-I. Wu, L. Li, L.-J. Chen, J.-H. He. *Monolayer MoS_2 Heterojunction Solar Cells.* ACS nano **8** (2014) 8317.
doi:10.1021/nn502776h

[3] K. S. Novoselov, A. K. Geim, S. V. Morozov, D. Jiang, Y. Zhang, S. V. Dubonos, I. V. Grigorieva, A. A. Firsov. *Electric Field Effect in Atomically Thin Carbon Films.* Science **306** (2004) 666.
doi:10.1126/science.1102896

[4] K. F. Mak, C. Lee, J. Hone, J. Shan, T. F. Heinz. *Atomically Thin* MoS_2*: A New Direct-Gap Semiconductor.* Phys. Rev. Lett. **105** (2010) 136805.
doi:10.1103/PhysRevLett.105.136805

[5] A. Ramirez-Torres, D. Le, T. S. Rahman. *Effect of monolayer supports on the electronic structure of single-layer MoS_2.* IOP Conference Series: Materials Science and Engineering **76** (2015) 012011.
doi:10.1088/1757-899x/76/1/012011

[6] J. Sun, Y. Choi, Y. J. Choi, S. Kim, J.-H. Park, S. Lee, J. H. Cho. *2D–Organic Hybrid Heterostructures for Optoelectronic Applications.* Advanced Materials **31** (2019) 1803831.
doi:10.1002/adma.201803831

[7] H. Shu, Y. Li, X. Niu, J. Wang. *Greatly Enhanced Optical Absorption of a Defective MoS_2 Monolayer through Oxygen Passivation.* ACS Applied Materials & Interfaces **8** (2016) 13150.
doi:10.1021/acsami.6b03242. PMID: 27144902

[8] J. P. Perdew, K. Burke, M. Ernzerhof. *Generalized Gradient Approximation Made Simple.* Phys. Rev. Lett. **77** (1996) 3865.
doi:10.1103/PhysRevLett.77.3865

[9] D. Sholl, J. Steckel. *Density Functional Theory - A practical introduction.* Wiley, Hoboken, 2009.

[10] P. Hohenberg, W. Kohn. *Inhomogeneous Electron Gas.* Phys. Rev. **136** (1964) B864.
doi:10.1103/PhysRev.136.B864

[11] W. Kohn, L. J. Sham. *Self-Consistent Equations Including Exchange and Correlation Effects.* Phys. Rev. **140** (1965) A1133.
doi:10.1103/PhysRev.140.A1133

[12] E. Kaxiras. *Atomic and Electronic Structure of Solids.* Cambridge University Press, 2003.
doi:10.1017/CBO9780511755545

[13] D. Bohm, D. Pines. *A Collective Description of Electron Interactions. I. Magnetic Interactions.* Phys. Rev. **82** (1951) 625.
doi:10.1103/PhysRev.82.625

[14] D. Pines, D. Bohm. *A Collective Description of Electron Interactions: II. Collective* vs *Individual Particle Aspects of the Interactions*. Phys. Rev. **85** (1952) 338. doi:10.1103/PhysRev.85.338

[15] D. Bohm, D. Pines. *A Collective Description of Electron Interactions: III. Coulomb Interactions in a Degenerate Electron Gas*. Phys. Rev. **92** (1953) 609. doi:10.1103/PhysRev.92.609

[16] L. Hedin. *New Method for Calculating the One-Particle Green's Function with Application to the Electron-Gas Problem*. Phys. Rev. **139** (1965) A796. doi:10.1103/PhysRev.139.A796

[17] D. Nabok, A. Gulans, C. Draxl. *Accurate all-electron G_0W_0 quasiparticle energies employing the full-potential augmented plane-wave method*. Phys. Rev. B **94** (2016) 035118. doi:10.1103/PhysRevB.94.035118

[18] M. S. Hybertsen, S. G. Louie. *Electron correlation in semiconductors and insulators: Band gaps and quasiparticle energies*. Phys. Rev. B **34** (1986) 5390. doi:10.1103/PhysRevB.34.5390

[19] C. Kittel. *Introduction to Solid State Physics*. Wiley, 2004.

[20] E. E. Salpeter, H. A. Bethe. *A Relativistic Equation for Bound-State Problems*. Phys. Rev. **84** (1951) 1232. doi:10.1103/PhysRev.84.1232

[21] W. Hanke, L. J. Sham. *Many-particle effects in the optical spectrum of a semiconductor*. Phys. Rev. B **21** (1980) 4656. doi:10.1103/PhysRevB.21.4656

[22] G. Strinati. *Application of the Green's functions method to the study of the optical properties of semiconductors*. Nuovo Cimento Rivista Serie **11** (1988) 1. doi:10.1007/BF02725962

[23] M. Rohlfing, S. G. Louie. *Electron-hole excitations and optical spectra from first principles*. Phys. Rev. B **62** (2000) 4927. doi:10.1103/PhysRevB.62.4927

[24] A. Fetter, J. Walecka. *Quantum Theory of Many Particle Systems*. McGraw-Hill Book Company, 1971.

[25] G. Onida, L. Reining, A. Rubio. *Electronic excitations: density-functional versus many-body Green's-function approaches*. Rev. Mod. Phys. **74** (2002) 601. doi:10.1103/RevModPhys.74.601

[26] F. Bechstedt. *Many-Body Approach to Electronic Excitations*, volume 181. Springer Berlin, 2015. doi:10.1007/978-3-662-44593-8

[27] M. S. Dresselhaus. *SOLID STATE PHYSICS - Optical Properties of Solids*. `http://web.mit.edu/course/6/6.732/www/6.732-pt2.pdf`. Accessed: 2020-08-27.

[28] J. Slater. *Wave Functions in a Periodic Potential*. Phys. Rev. **51** (1937) 846. doi:10.1103/PhysRev.51.846

[29] J. Slater. *Energy Band Calculations by the Augmented Plane Wave Method.* Advances in Quantum Chemistry **1** (1964) 35.
doi:10.1016/S0065-3276(08)60374-3

[30] T. Loucks. *Augmented Plane Wave Method: A Guide to Performing Electronic Structure Calculations.* Frontiers in Physics: Lecture note and reprint series, A. W.A. Benjamin, 1967.

[31] D. Singh. *Planewaves, Pseudopotentials and the LAPW Method.* Springer Science+Business Media, Inc., New York, 2002.

[32] O. Andersen. *Ground-state properties of lanthanum: Treatment of extended-core states.* Phys. Rev. B **12** (1975) 3060.
doi:10.1103/PhysRevB.12.3060

[33] D. Singh. *Energy Band Calculations by the Augmented Plane Wave Method.* Phys. Rev. B **43** (1991) 6388.
doi:10.1103/PhysRevB.43.6388

[34] E. Sjöstedt, L. Nordström, D. J. Singh. *An alternative way of linearizing the augmented plane-wave method.* Solid State Communications **114** (2000) 15.
doi:10.1016/S0038-1098(99)00577-3

[35] A. Gulans, S. Kontur, C. Meisenbichler, D. Nabok, P. Pavone, S. Rigamonti, S. Sagmeister, U. Werner, C. Draxl. *exciting: a full-potential all-electron package implementing density-functional theory and many-body perturbation theory.* J. Phys: Condens. Matter **26** (2014) 363202.
doi:10.1088/0953-8984/26/36/363202

[36] P. A. Young. *Lattice parameter measurements on molybdenum disulphide.* Journal of Physics D: Applied Physics **1** (1968) 936.
doi:10.1088/0022-3727/1/7/416

[37] H. J. Monkhorst, J. D. Pack. *Special points for Brillouin-zone integrations.* Phys. Rev. B **13** (1976) 5188.
doi:10.1103/PhysRevB.13.5188

[38] F. A. Rasmussen, K. S. Thygesen. *Computational 2D Materials Database: Electronic Structure of Transition-Metal Dichalcogenides and Oxides.* The Journal of Physical Chemistry C **119** (2015) 13169.
doi:10.1021/acs.jpcc.5b02950

[39] `http://exciting-code.org/nitrogen-excited-states-from-bse`. Accessed: 2020-08-21.

[40] J. P. Perdew. *Density functional theory and the band gap problem.* International Journal of Quantum Chemistry **28** (1985) 497.
doi:https://doi.org/10.1002/qua.560280846

[41] S. Edalati-Boostan, C. Cocchi, C. Draxl. *MoTe2 as a natural hyperbolic material across the visible and the ultraviolet region.* Physical Review Materials **4** (2020).
doi:10.1103/physrevmaterials.4.085202

[42] Y.-C. Zhou, H.-L. Zhang, W.-Q. Deng. *A 3N rule for the electronic properties of doped graphene.* Nanotechnology **24** (2013) 225705.
doi:10.1088/0957-4484/24/22/225705

[43] F. Hüser, T. Olsen, K. S. Thygesen. *How dielectric screening in two-dimensional crystals affects the convergence of excited-state calculations: Monolayer MoS_2.* Phys. Rev. B **88** (2013) 245309.
doi:10.1103/PhysRevB.88.245309

[44] H. Shi, H. Pan, Y.-W. Zhang, B. I. Yakobson. *Quasiparticle band structures and optical properties of strained monolayer MoS_2 and WS_2.* Phys. Rev. B **87** (2013) 155304.
doi:10.1103/PhysRevB.87.155304

[45] T. Cheiwchanchamnangij, W. R. L. Lambrecht. *Quasiparticle band structure calculation of monolayer, bilayer, and bulk MoS_2.* Phys. Rev. B **85** (2012) 205302.
doi:10.1103/PhysRevB.85.205302

[46] D. Y. Qiu, F. H. da Jornada, S. G. Louie. *Optical Spectrum of MoS_2: Many-Body Effects and Diversity of Exciton States.* Phys. Rev. Lett. **111** (2013) 216805.
doi:10.1103/PhysRevLett.111.216805

[47] F. Bassani, G. P. Parravicini. *Band structure and optical properties of graphite and of the layer compounds GaS and GaSe.* Nuovo Cimento B Serie **50** (1967) 95.
doi:10.1007/BF02710685